



## RESEARCH ARTICLE

10.1002/2016JA023719

## Key Points:

- ~1 MeV electrons can be injected into the inner zone during large storms, forming new belts that decay very slowly
- 0.7–1.5 MeV electrons that are transported into the slot region decay rapidly (~10 days)
- We find no evidence of electrons >1.5 MeV in the inner zone during the interval considered (April 2013 through September 2016)

## Supporting Information:

- Supporting Information S1

## Correspondence to:

S. G. Claudepierre,  
sethclaudpierre@gmail.com

## Citation:

Claudepierre, S. G., et al. (2017), The hidden dynamics of relativistic electrons (0.7–1.5 MeV) in the inner zone and slot region, *J. Geophys. Res. Space Physics*, 122, doi:10.1002/2016JA023719.

Received 23 NOV 2016

Accepted 7 FEB 2017

## The hidden dynamics of relativistic electrons (0.7–1.5 MeV) in the inner zone and slot region

S. G. Claudepierre<sup>1</sup>, T. P. O'Brien<sup>1</sup>, J. F. Fennell<sup>1</sup>, J. B. Blake<sup>1</sup>, J. H. Clemmons<sup>1</sup>, M. D. Looper<sup>1</sup>, J. E. Mazur<sup>1</sup>, J. L. Roeder<sup>1</sup>, D. L. Turner<sup>1</sup>, G. D. Reeves<sup>2</sup>, and H. E. Spence<sup>3</sup>
<sup>1</sup>Space Sciences Department, The Aerospace Corporation, El Segundo, California, USA, <sup>2</sup>Space and Atmospheric Sciences Group, Los Alamos National Laboratory, Los Alamos, New Mexico, USA, <sup>3</sup>Institute for the Study of Earth, Oceans, and Space, University of New Hampshire, Durham, New Hampshire, USA

**Abstract** We present measurements of relativistic electrons (0.7–1.5 MeV) in the inner zone and slot region obtained by the Magnetic Electron and Ion Spectrometer (MagEIS) instrument on Van Allen Probes. The data presented are corrected for background contamination, which is primarily due to inner-belt protons in these low- $L$  regions. We find that ~1 MeV electrons were transported into the inner zone following the two largest geomagnetic storms of the Van Allen Probes era to date, the March and June 2015 events. As ~1 MeV electrons were not observed in Van Allen Probes data in the inner zone prior to these two events, the injections created a new inner belt that persisted for at least 1.5 years. In contrast, we find that electrons injected into the slot region decay on much faster timescales, approximately tens of days. Furthermore, we find no evidence of >1.5 MeV electrons in the inner zone during the entire time interval considered (April 2013 through September 2016). The energies we examine thus span a transition range in the steeply falling inner zone electron spectrum, where modest intensities are observed at 0.7 MeV, and no electrons are observed at 1.5 MeV. To validate the results obtained from the background corrected flux measurements, we also present detailed pulse-height spectra from individual MagEIS detectors. These measurements confirm our results and also reveal low-intensity inner zone and slot region electrons that are not captured in the standard background corrected data product. Finally, we briefly discuss efforts to refine the upper limit of inner zone MeV electron flux obtained in earlier work.

## 1. Introduction

Due to the intense penetrating proton radiation present in the inner zone, the actual electron dynamics are often obscured either by intense background contamination or merely by lack of confidence that the measurements are sufficiently background free. Using the unique capabilities of the Magnetic Electron and Ion Spectrometer (MagEIS) [Blake et al., 2013] on the Van Allen Probes mission [Mauk et al., 2013], we explore newly revealed dynamics of 0.7–1.5 MeV electrons in the inner zone and slot region. Throughout this work, we refer to the outer zone as  $L > 3$ , the inner zone as  $L < 2$ , and the slot region as  $L = 2-3$ , noting however that these definitions are energy dependent [Reeves et al., 2016] and that the inner zone/slot distinction is a consequence of the different electron lifetimes in these two regions. Claudepierre et al. [2015] describe the automated background subtraction procedure used in standard MagEIS data postprocessing. This method involves interpolating the background count rate across the energy passband of the magnetic filter. In the present work, we also utilize high-energy resolution data provided by MagEIS to gain additional insights into the dynamics of these hidden particles. Before we proceed, we briefly review the current state of knowledge regarding inner zone electron dynamics.

Cladis et al. [1973] and Schulz and Lanzerotti [1974] provide excellent reviews of the radiation belt literature from the first decades of the space age. Rosen and Sanders [1971] describe a dynamic inner zone with rapid enhancements followed by slow decays, while Lyons and Thorne [1973] describe the equilibrium structure of the electron radiation belts in terms of a balance between inward radial diffusion from the plasma sheet [Newkirk and Walt, 1968a; Tomassian et al., 1972] and pitch-angle scattering into the atmosphere. Bostrom et al. [1970] consider a 5 year time interval in the 1960s and argue that there are no electrons with energies greater than 1.2 MeV below  $L = 3$ , while West and Buck [1976] show that the inner zone electron energy spectrum is very steep. And at very low  $L$  (<1.2), it appears that the radial gradient of the radial diffusion

©2017. The Authors.

This is an open access article under the terms of the Creative Commons Attribution-NonCommercial-NoDerivs License, which permits use and distribution in any medium, provided the original work is properly cited, the use is non-commercial and no modifications or adaptations are made.

coefficient changes sign, from positive to negative, such that the coefficient increases as  $L$  decreases toward the atmosphere [Newkirk and Walt, 1968b; Farley, 1969].

Many of the results from the 1960s and 1970s have been reconfirmed with Van Allen Probes data. *Li et al.* [2015] provide an estimate of the upper limit of MeV electron flux based on known backgrounds in the Relativistic Electron Proton Telescope instrument on Van Allen Probes. *Fennell et al.* [2015] show that there are no MeV electrons detectable in the inner zone in the early part of the Van Allen Probes mission (through February 2013) using the MagEIS instrument and that the spectrum is very steep at relativistic energies. *O'Brien et al.* [2016] confirm the prior estimates of the quiet time radial diffusion coefficient in the inner zone.

As noted above, inner zone electron dynamics are typically attributed to radial diffusion and atmospheric loss. However, *Albert et al.* [2016] claim that radial diffusion may be negligible, with the dominant mechanism governing dynamics and morphology being energy-angle diffusion by VLF waves. This claim is motivated by the MagEIS observations reported by *Zhao et al.* [2014a, 2014b], which describe pitch-angle distributions in the inner belt with peaks away from  $90^\circ$ , suggesting that some additional process (radial or energy diffusion) acts faster than pitch-angle diffusion.

Other recent studies have sought to improve models of specific physical processes in the inner zone. *Selesnick* [2012, 2016] provide updated loss estimates using numerical simulations of electron-atmosphere interactions. *Selesnick* [2015a] investigates the Cosmic Ray Albedo Neutron Decay (CRAND) as an inner zone electron source mechanism and concludes that CRAND is likely not the dominant source of electrons below 1–2 MeV but might be dominant above 2 MeV. Consistent with most prior work, *Selesnick* [2015a] speculates that radial diffusion supplies the <2 MeV population. *Selesnick* [2015b] revisited the Solar Anomalous and Magnetospheric Particle Explorer low-altitude electron observations and concludes the data in the inner zone are often heavily contaminated by chance coincidences between lower energy electrons and high-energy protons. However, in quasi-trapped regions below the mirror points of the stable proton belt, the author is able to identify fluxes at 1 MeV that are 2–3 orders of magnitude lower than those at 0.5 MeV as well as fluxes at  $\sim 1.5$  MeV that are lower still by 3–4 orders of magnitude (the reported  $e$ -folding energy is  $\sim 100$  keV). This sharp dropoff in flux is in agreement with an extrapolation (to higher energies) of the flux spectrum published in *Fennell et al.* [2015] but is softer than the CRAND spectrum computed by *Selesnick* [2015a].

There has been a renewed interest in identifying the source mechanism(s) responsible for inner zone electron enhancements, due in large part to the high-quality data from the Van Allen Probes. *Zhao and Li* [2013] use a 1-D radial diffusion code to explain episodic enhancements of inner zone electron fluxes with hundreds of keV energy. *Selesnick et al.* [2016] show that local time asymmetry in the 100–400 keV inner zone electrons is consistent with the large-scale electric field influence on the electron drift orbits. Using the  $K_p$  index as a proxy for electric field strength, they show that electrostatic radial diffusion is adequate to explain storm-time enhancements as radial transport. Conversely, *Su et al.* [2016] show rapid convective injection by a sudden large change in the electric field, inferred from a jump in  $K_p$ . Using Van Allen Probes data, *Turner et al.* [2015] explore substorm-associated injections in 2013 that reach as deep as  $L \sim 2.5$ . Such injections can, for example, enhance the “outer boundary” of the inner zone for subsequent inward radial diffusion.

A common theme through most of these studies is that  $\sim$ MeV electrons in the inner zone and slot region are elusive: they have very low fluxes and are transient. In what follows, we investigate the dynamics of these particles with the high-quality measurements from the MagEIS instrument on Van Allen Probes. The quantification and removal of inner-belt proton contamination in these data reveals the hidden dynamics of the inner zone and slot region electrons. The remainder of this paper is structured as follows. In section 2, we present an overview of the MagEIS instrument, the data products that will be used, and the standard background correction method. Section 3 presents a detailed analysis of the 0.7–1.5 MeV electron data in the innermost regions of the Earth’s magnetosphere. In section 4, we attempt to quantify more precisely the upper limit of  $\sim$ MeV electron flux in the inner zone provided by *Fennell et al.* [2015]. Finally, in section 5, we summarize and offer concluding remarks.

## 2. Instrumentation and Data

In the following subsections, we provide a high-level summary of the MagEIS sensor on the Van Allen Probes, highlighting the details most pertinent for the current work. The interested reader is referred to *Blake et al.* [2013] for a more in-depth treatment.

## 2.1. The MagEIS Instrument

NASA's Van Allen Probes mission consists of two identically instrumented spacecraft orbiting the Earth in near-equatorial, geostationary transfer orbits. The primary goal of the mission is to elucidate the physical processes responsible for the energization, transport, and loss of radiation belts electrons. The mission launched on 30 August 2012 and continues to operate, with the majority of the instruments performing nominally. The highly elliptical orbit extends nearly to the geosynchronous region, with an apogee of  $\sim 5.8 R_E$  (geocentric) and a perigee at roughly 600 km altitude above the Earth's surface. The orbital period is approximately 9 h, sweeping the Van Allen Probes through the radiation belt region 5–6 times per day. The spacecraft spin with a period of  $\sim 11$  s, providing directional particle measurements over  $0$ – $360^\circ$  local pitch angle on this time cadence.

Each of the twin Van Allen Probe spacecraft is equipped with four individual MagEIS units, which measure energetic electrons in the near-Earth space environment. We refer to these four units as LOW, M35, M75, and HIGH, designations chosen to indicate the electron energy coverage of each unit. The LOW unit measures electrons from  $\sim 20$ – $200$  keV, the M35 and M75 units measure medium-energy electrons from  $\sim 200$  to  $1000$  keV, and the HIGH unit measures electrons from  $\sim 1$  to  $4$  MeV. The M35 and M75 units are identical apart from their orientation with respect to the spacecraft spin axis, where M75 points in the same direction as the LOW and HIGH units, at an angle of  $75^\circ$  from the axis, and M35 points at  $35^\circ$  from the axis. As the two medium units are redundant in terms of their energy coverage, here we only report measurements from the M75 unit. The MagEIS HIGH unit also houses an ion range telescope that measures energetic protons and heavier ions, but we do not discuss MagEIS ion measurements in the present work.

The MagEIS instrument uses a magnetic deflection measurement technique, where a nearly constant magnetic field is maintained within the instrument housing. This field deflects electrons, via the Lorentz force, through  $180^\circ$  toward an array of silicon-solid state detectors, while ions are deflected in the opposite direction, away from the detectors, toward the side and back walls of the unit. The LOW and M75 units each use a single array of nine detectors, or “pixels,” while the HIGH unit uses an array of 4 pixels. Each individual pixel in the HIGH unit consists of multiple-stacked detectors, where the increased thickness is needed to stop the higher-energy electrons within the stack. The HIGH unit also uses coincidence between the front and rear detectors in each pixel stack. Incident electrons deposit their energy within the detectors, which generates a charge pulse that is recorded as digitized pulse heights. The pulse-height spectrum is recorded for each pixel over a range of 256 pulse-height channels, which is downsampled via onboard look-up tables (LUTs) to 64 channels. This downsampling is done before the data are telemetered to the ground, to fit within telemetry rate limitations. We note that the downsampling is produced from the pulse-height channels in the neighborhood of the peak in the magnetic filter response. For example, rather than using a uniform 4-to-1 mapping from the 256 pulse-height channels into the 64 channels, we instead use our a priori knowledge of where the peak response is in the 256 pulse-height channel space. (This knowledge was obtained via preflight laboratory calibrations). Thus, we downsample a subset of the 256 channels that lie in the neighborhood of the peak response, typically in a 2-to-1 mapping (i.e., we downsample only the 128 pulse-height channels that surround the peak response). We refer to these downsampled 64 channels as the “histogram” channels and the corresponding pulse-height data as the histogram data, as opposed to the “main channel” data (which is described below) that report one value representing the entire energy-deposit range sampled by each pixel (or two values for most HIGH pixels).

The 64-channel histogram data are recorded at a coarser time cadence and angular resolution than the main channel data, again, due to telemetry limitations. The histogram data time cadence and angular resolution are configurable via commanding and are typically set to be two times coarser than the main channel data. The histogram data are telemetered continuously in the “normal” mode of MagEIS operations, though it is not telemetered in the “high rate” mode [see *Claudepierre et al.*, 2015, and below]. MagEIS is operated such that it is essentially always in the normal mode (recording histogram data) in the inner zone.

## 2.2. MagEIS Histogram Data

Figure 1 demonstrates the MagEIS measurement technique described above. Detector counts are shown versus histogram channel from pixel 6 from the M75 unit on Van Allen Probe B. These counts were accumulated very close to the geomagnetic equator for approximately 1000 days (1 April 2013 through 31 December 2015) in the  $L$  range from 4.4–4.6 and over the range of local pitch angles,  $\alpha$ , from  $80$  to  $100^\circ$ . The *Olson and Pfizter* [1977] quiet magnetic field model is used throughout this work to calculate the  $L$  parameter on the

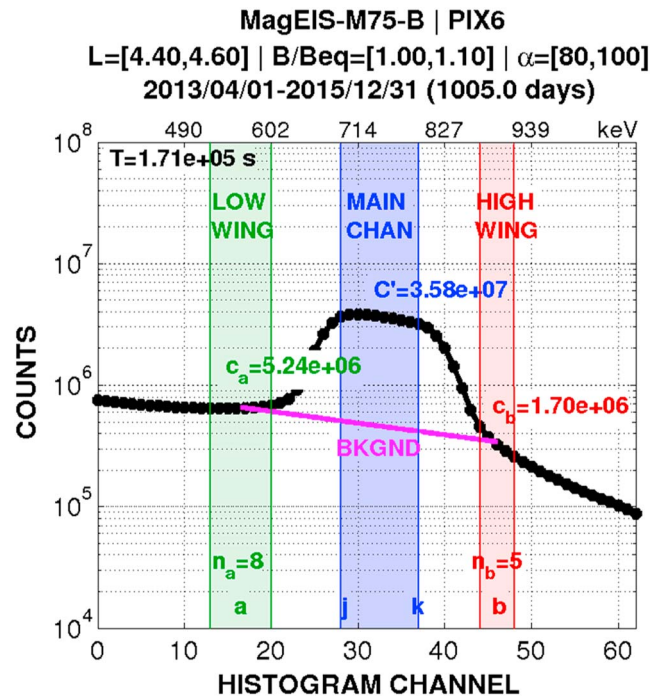


**Figure 1.** MagEIS histogram data from M75 pixel 6 (counting from zero) on Van Allen Probe B, in the indicated  $L$ ,  $B/B_{eq}$ , and local pitch-angle ( $\alpha$ ) range. The data were accumulated in this range over a roughly 1000 day interval, which reduces to  $\sim 2$  total days of data meeting the selection criteria. The peak in the histogram profile is due to the action of momentum selection by the instrument's magnetic field, steering particles within a narrow energy range onto the detector. This main channel passband is indicated (between channels  $j$  and  $k$ ), along with the low and high wings, where the counts registered are primarily due to background. The magenta line thus approximates the background in the main channel passband. The labeled parameters are the same as in *Claudepierre et al.* [2015]:  $a$  is the center channel of the low wing;  $b$  is the center channel of the high wing;  $j$  is the left channel of the main channel passband;  $k$  is the right channel of the main channel passband;  $c_a$  is the total (summed) counts in the  $n_a$  low-wing channels;  $c_b$  is the total counts in the  $n_b$  high-wing channels;  $C'$  is the total counts in the main channel passband; and  $T$  is the total accumulation time.

centroid of the channel passband) in the MagEIS data files, with counts converted to unidirectional, differential electron flux in the usual manner. We note, however, that this summing to create the main channels is done on board on the full 256 channel pulse-height spectrum, before it is downsampled to the 64 histogram channels. For the LOW and MED (M35 or M75) units, one main channel is created from each pixel 2–8 (pixels 0 and 1 are noisy and are not used) to produce 7 total main channels (which we number 2–8) from a given LOW/MED unit. The four HIGH unit pixels are subdivided into seven energy channels, with pixel 0 contributing to HIGH unit main channel 0, while each of pixels 1–3 is split into two main channels. Specifically, HIGH pixel 1 is split into main channels 1 and 2, pixel 2 is split into main channels 3 and 4, and pixel 3 is split into main channels 5 and 6.

The histogram data are useful for quantifying background contamination in the main channel electron measurements. Very energetic particles, such as inner-belt protons, can penetrate the instrument shielding from all directions and register as valid counts in a detector. Thus, any counts outside of the main channel passband are considered background. In Figure 1, we highlight the “low-wing” and “high-wing” histogram channels, which delineate the regions of the pulse-height spectrum influenced by penetrating backgrounds. We note that backscatter likely also contributes to the low-wing counts [*Claudepierre et al.*, 2015], as some fraction of the incident particles do not deposit their full energy within the detector. They can “backscatter” out of the incident plane, or exit through the sides of the detector, before fully stopping within the detector. As these

spacecraft trajectory, along with the ratio of the magnetic field strength at the spacecraft location to the equatorial field strength ( $B/B_{eq}$ ). The total integration time in this region of  $L$ ,  $B/B_{eq}$ , and  $\alpha$  space is  $\sim 1.71 \times 10^5$  s ( $\sim 2$  days). Note the peak in the histogram data profile between histogram channels 28–38, with a relatively flat profile in these channels when compared with the sharp gradients on either side. The shape of this profile is due to the action of the momentum selection within the magnetic spectrometer, which preferentially steers particles over a narrow energy range onto the pixel. The main energy channel passband, labeled “MAIN CHAN,” was determined via preflight calibrations to be 692–793 keV (the energy values for a given histogram channel are shown on the top horizontal scale). The histogram counts in a given histogram channel within the main channel passband are roughly  $4 \times 10^6$ , indicating a count rate on the order of 20 counts/s per histogram channel.

The main channel data that are reported in the publicly available MagEIS data files are created from these high-resolution pulse-height spectra via another set of onboard LUTs, as follows. For a given pixel, the counts are first summed in the main channel passband, as defined by the LUT. For example, in Figure 1, the counts are summed from histogram channel  $j$  to channel  $k$ , to produce the total counts in the main channel passband,  $C'$ . This value is reported as the flux at 750 keV (the



particles do not deposit their full energy in the detector, they show up as counts in the low wing, an effect that we have measured in preflight laboratory testing. The low-wing and high-wing locations are determined for each pixel on each unit by visually inspecting  $L$ -binned histogram data in regions of space where backgrounds are believed to be low (e.g., the outer zone, when ultrarelativistic electron fluxes are low).

An estimate of the background in the main channel is shown by the magenta line in Figure 1, which is a simple linear interpolation between the low- and high-wing counts. We can then subtract the background counts summed in the channel passband from the main channel counts to arrive at the background corrected counts. This is a simplified description of the full procedure used to correct the main channel data for background contamination, which is described in greater detail in *Claudepierre et al.* [2015]. In what follows, we refer to this as the “standard” background correction algorithm. The various histogram parameters in Figure 1 ( $a$ ,  $c_a$ , etc.) are defined in the figure caption and are the same as used in *Claudepierre et al.* [2015].

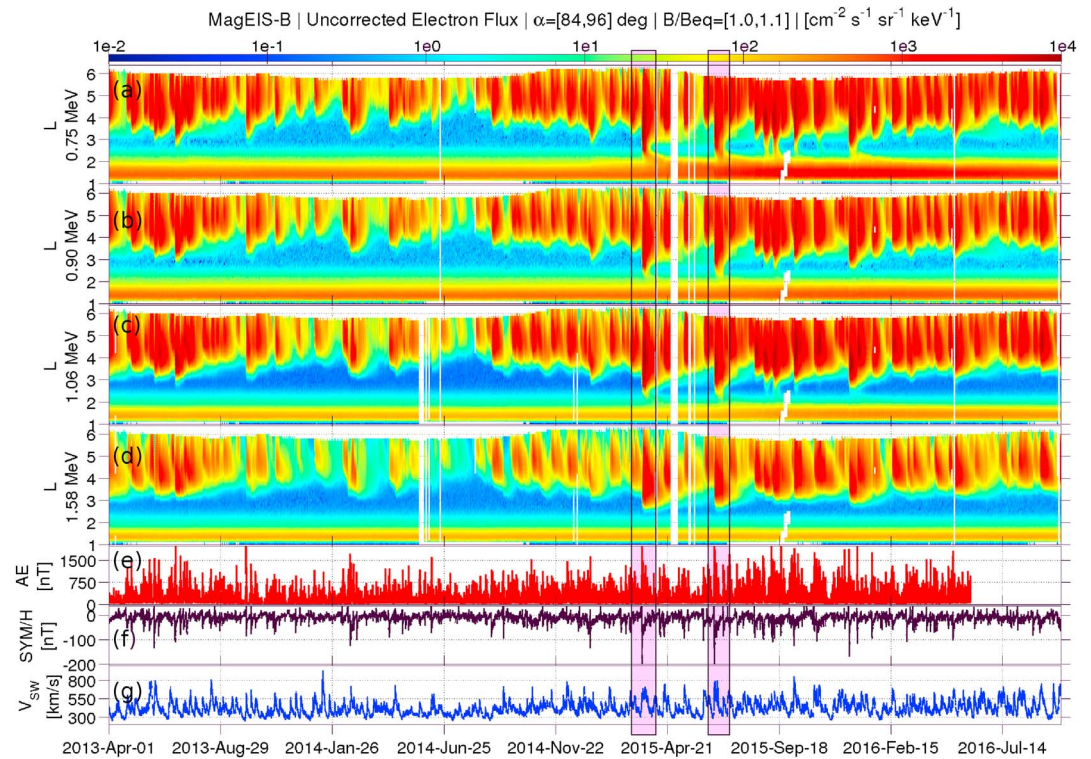
### 2.3. MagEIS Main Channel Data With Standard Background Corrections

Figure 2 shows uncorrected MagEIS-B daily-averaged electron fluxes in  $L$ -versus-time format for four main energy channels: 0.75, 0.90, 1.06, and 1.58 MeV (Figures 2a–2d, respectively). The displayed time interval, 1 April 2013 through 30 September 2016, is used throughout this study. We focus on this time interval because it represents a uniform set of MagEIS data, with relatively few instrument configuration changes when compared with the numerous changes that occurred early in the mission (e.g., prior to 1 April 2013). In the figure, the first two energy channels, 0.75 and 0.90 MeV, are main channels 6 and 7 from the MagEIS-B M75 unit (pixels 6 and 7, respectively), while 1.06 and 1.58 MeV are main channels 0 and 1 from the HIGH unit (pixel 0 and the first half of pixel 1, respectively). These MagEIS data are extracted very near the magnetic equator ( $B/B_{eq} < 1.1$ ) and centered on 90 degrees local pitch angle ( $\alpha = [84, 96]$  degrees). We note that this local pitch angle and  $B/B_{eq}$  range maps to roughly 70–110° equatorial pitch angle. For context, Figures 2e–2g show 5 min OMNI values of  $AE$ ,  $SYM-H$ , and solar wind speed ( $v_{sw}$ ), respectively. Note that outer radiation belt flux enhancements at these energies generally follow the trends in activity and driving conditions, with flux enhancements correlated with increased  $AE$  activity, for example. We also note that the two highlighted events, March and June 2015, appear to result in 0.75 MeV electron penetration through the slot region and into the inner zone (Figure 2a). However, in these uncorrected data, we cannot be certain which inner zone and slot features are valid and which are due to inner-belt proton contamination.

Figure 3 shows MagEIS-B daily-averaged electron fluxes with the standard background correction algorithm applied, in the same format as Figure 2. The data gaps in the 0.75 and 0.90 MeV channels early in the time interval at  $L > 3$  are due to the operation of the M75 unit in “high rate” mode. In this mode, histogram data are not telemetered in favor of additional main-channel measurements recorded at a very high time cadence [e.g., *Fennell et al.*, 2014]. Thus, the background corrections are not possible during these times, as they require the histogram data. We also note that pixel 8 on M75 measures fluxes at  $\sim 1$  MeV, which provides overlap with the pixel 0 channel from the HIGH unit (1.06 MeV, Figure 2c). However, it is not possible, at present, to use the histogram data from M75 pixel 8 to estimate the background, so that background corrections are not possible on this channel. Thus, this  $\sim 1$  MeV channel from M75 is not shown in either Figure 2 or Figure 3. The interested reader is referred to *Claudepierre et al.* [2015] for a more complete description of the standard background correction algorithm and the caveats and limitations thereon.

Comparing Figure 2 and Figure 3 reveals several features of note. First, in all four channels, the outer zone fluxes are essentially the same in both figures, indicating that background contamination is minimal in this region. However, there are intervals where subtle differences in the outer zone can be seen, due to bremsstrahlung radiation contamination from ultrarelativistic electrons ( $\sim 5$  MeV; see *Claudepierre et al.*, 2015]. For example, in Figure 3c between March 2015 and June 2015, note that the inner edge of the outer zone steadily moves to higher  $L$ , while in the uncorrected data, it remains at essentially the same  $L$  ( $L \approx 2.8$ ). We also note that the correction algorithm does not fully remove this Bremsstrahlung contamination from the M75 channels (Figures 3a and 3b) during this interval of enhanced ultrarelativistic electron flux near  $L \approx 3$  [e.g., *Baker et al.*, 2016].

The second feature of note is revealed by comparing the uncorrected and corrected fluxes at 0.75 MeV (Figures 2a and 3a), where the background corrected fluxes provide a more accurate characterization of the inner zone and slot region electron dynamics. For example, in Figure 2a, we see an intense flux signature near  $L = 1.4$  that remains centered at this  $L$  for the entire interval shown and increases in both  $L$ -width and intensity



**Figure 2.** (a–d) Uncorrected MagEIS-B daily-averaged electron fluxes plotted in  $L$ -versus-time format. These data have not been corrected for background contamination. Four energy channels are shown: 0.75, 0.90, 1.06, and 1.58 MeV, respectively. The 0.75 and 0.90 MeV energy channels are from the MagEIS-B M75 unit, while the 1.06 and 1.58 MeV channels are from the HIGH unit. These data are extracted very near the magnetic equator ( $B/B_{eq} < 1.1$ ) and centered on  $90^\circ$  local pitch angle ( $\alpha = [84, 96]$  degrees). Occasional data gaps exist, and the missing data at  $L < 3$  in September 2015 is due to the inadvertent operation of the calibration pulser. (e–g) Five minutes OMNI values of AE, SYM-H, and solar wind speed, respectively. The March and June 2015 storm events are highlighted across all of the panels.

following the March and June 2015 events. However, in Figure 3a, we see that once the correction algorithm has been applied, the flux intensity near  $L = 1.4$  has decreased by roughly 1 order of magnitude when compared with the uncorrected data, up until March 2015. After this time, the inner zone fluxes have roughly the same intensity in both the corrected and uncorrected data. As we demonstrate below, the intense fluxes near  $L = 1.4$  prior to March 2015 in the uncorrected data are strongly influenced by contamination from inner zone protons. Once the corrections have been applied, the inner zone flux is substantially reduced in the corrected data, prior to March 2015. After March 2015, both the 17 March 2015 and 23 June 2015 geomagnetic storms [Baker et al., 2016] led to 0.75 MeV electron flux enhancements in the inner zone. In these instances, the inner zone flux enhancements are large relative to the proton contamination, thus giving similar intensities in Figures 2a and 3a.

The third feature of note is revealed by comparing the uncorrected and corrected fluxes at 0.90 MeV (Figures 2b and 3b), where the electrons dynamics are similar to the 0.75 MeV electrons. However, in Figure 3b, once the correction algorithm has been applied, we see that there are essentially no 0.90 MeV electrons above the MagEIS detection threshold near  $L = 1.4$  prior to March 2015 [e.g., Fennell et al., 2015]. Again, after this time, the strong geomagnetic storms of March and June 2015 led to inner zone flux enhancements at this energy. In addition, in Figure 3b, we draw attention to the region of apparent enhanced flux between  $L = 2$  and 2.5. We demonstrate below that these are not real 0.90 MeV electrons and is the signature of residual contamination that is not entirely removed by the standard background correction algorithm (this is also discussed in Claudepierre et al. [2015]).

The fourth feature of note is revealed by comparing the uncorrected and corrected fluxes at 1.06 MeV (Figures 2c and 3c). Again, once the correction algorithm has been applied, there is no evidence of 1.06 MeV electrons in the inner zone until after the June 2015 storm. This event clearly results in electron transport

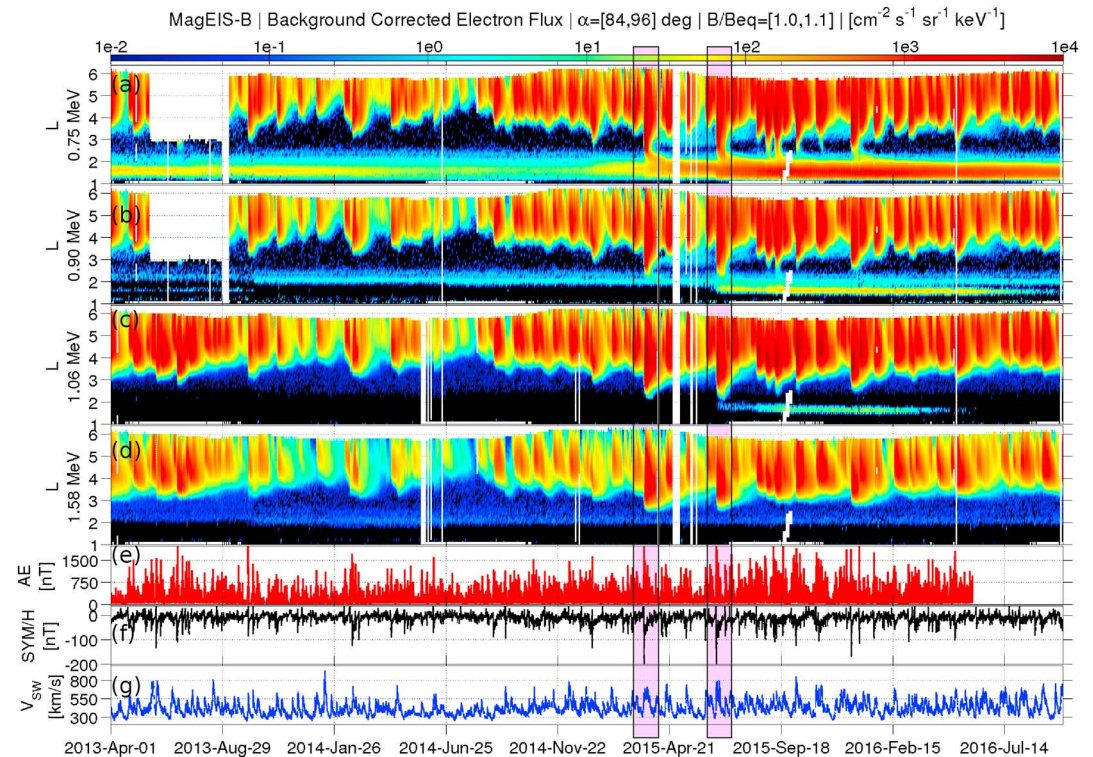


**Figure 3.** Same format as Figure 2, but here the data have been corrected for background contamination. Note in Figure 3c the substantial differences in the inner zone and slot region, when compared with Figure 2, including the otherwise hidden, newly formed  $\sim 1$  MeV inner belt.

through the slot region, with 1.06 MeV electrons penetrating into the inner zone. However, as we demonstrate below, electrons at this energy are also observed in the inner zone following the March 2015 event, albeit at very low intensities. This signature is not evident in the data produced using the standard background correction algorithm (Figure 3c), as the algorithm requires significant flux enhancements relative to the background in order to be effective.

The fifth feature of note is revealed by comparing the uncorrected and corrected fluxes at 1.58 MeV (Figures 2d and 3d). Here we see that no electrons are able to penetrate the inner zone or inner slot region for the entire interval shown. This suggests that no electrons are present in the inner zone at this energy, or that they are of very low intensity, below the detection threshold of the MagEIS HIGH unit. A similar result holds for the higher energy MagEIS channels (1.58–4 MeV, not shown here). We also see a faint band of residual contamination near  $L = 2$ , again entirely due to backgrounds not completely removed by the standard correction algorithm.

On the whole, Figure 3 suggests that electrons in the energy range 0.75–1.06 MeV that are transported into the slot region decay quite rapidly, on the order of 10 days, whereas electrons that traverse the slot and penetrate into the inner zone remain trapped there for a much longer time. For example, in Figure 3c, we see that the new inner belt created after the June 2015 event persists for a long time (on the order of 1 year), while the slot region electrons vanish within a couple of weeks after the event. We have computed  $e$ -folding times for the slot region decays and find values on the order of 1–5 days for 0.75–1.06 MeV electrons (not shown here), consistent with previous estimates [Fennell *et al.*, 2012].

We emphasize that many of the features described above regarding the dynamics of relativistic electrons in the inner zone and slot region are usually hidden by inner-belt proton contamination. The true dynamics are not revealed until the standard background correction has been applied. However, as will be evident below, the standard correction algorithm is not perfect and has limitations. Thus, we seek additional evidence to confirm or refute the presence of relativistic electrons in the inner zone and slot, as suggested by the data in Figure 3. This is the goal of section 3, where we consider the high-energy-resolution histogram data in detail.



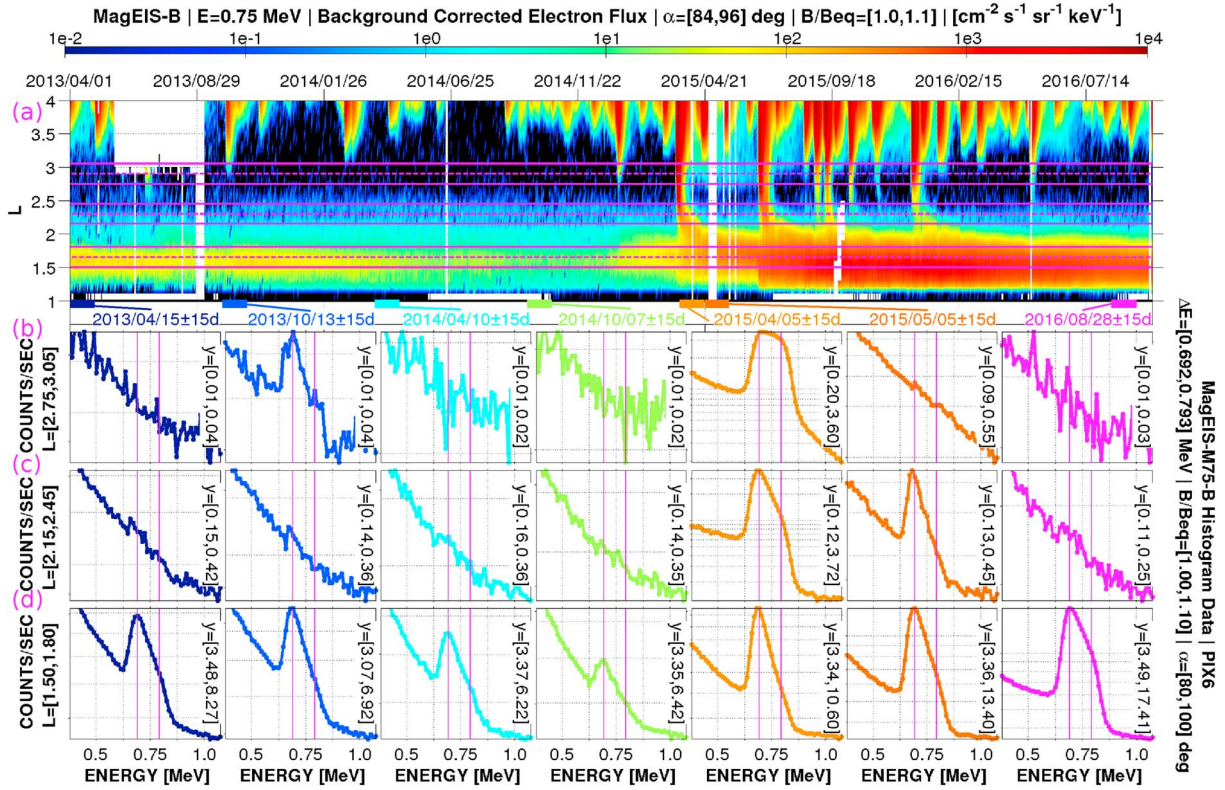


**Figure 4.** (a) MagEIS-B daily-averaged electron flux at 0.75 MeV from pixel 6 on the M75 unit (the same data as shown in Figure 3a). These background corrected data are plotted in  $L$ -versus-time format, with the time axis shown at the top of panel. Three  $L$  regions are highlighted:  $L = 2.75\text{--}3.05$ ,  $L = 2.15\text{--}2.45$ , and  $L = 1.50\text{--}1.80$ . The center of each  $L$  range is indicated by the dashed magenta line, and the edges are indicated by the solid magenta lines. (b–d) Histogram count rate profiles plotted versus energy, in each of the three  $L$  ranges (rows) and for the time intervals called out by colored bars at the bottom of Figure 4a (columns). The histogram counts are accumulated over 30 day windows, with the dates indicated at the top of the panels in Figure 4b and marked with bars below Figure 4a. These histogram data are only accumulated near the magnetic equator ( $B/B_{\text{eq}} < 1.1$ ) and over local pitch angles  $80\text{--}100^\circ$ . The vertical count-rate scale is different in each panel, with the range indicated at the right of each panel (" $y = [\dots]$ "). The main channel passband for this pixel,  $\Delta E = [0.692, 0.793]$  MeV, is shown with vertical magenta lines and indicated at the right of the figure.

### 3. Detailed Analysis With MagEIS Histogram Data

#### 3.1. Inner Zone and Slot Region Dynamics: 0.75 MeV

We begin with the 0.75 MeV channel shown in Figure 3a. Figure 4a presents the same data but zoomed in on the low- $L$  region ( $L < 4$ ). We examine the histogram data from this pixel (pixel 6) in detail in three  $L$  regions:  $L = 2.75\text{--}3.05$ ,  $L = 2.15\text{--}2.45$ , and  $L = 1.50\text{--}1.80$ . The center of each  $L$  range is indicated in Figure 4a by the dashed magenta line, and the edges are indicated by the solid magenta lines. The time axis is shown at the top of Figure 4a.

Figures 4b–4d show histogram count rates from this pixel plotted versus energy deposited, with the energy scale indicated below Figure 4d, in the three  $L$  ranges noted above. The different columns are different time intervals called out by colored bars at the bottom of Figure 4a. In what follows, we assume that the energy deposited represents the total incident energy of a particle (i.e., we label the axis "ENERGY" in Figures 4b–4d). The difference between energy deposited and incident energy is related to the backscatter process described above. An incident particle that fully stops within a detector deposits its full energy in that detector, and thus, the incident energy is equal to the energy deposited. However, some particles scatter back out of the incident plane of the detector or exit through the sides of the detector before depositing their full energy. Thus, in these cases, the incident energy is not equal to the energy deposited. Moreover, in the HIGH unit, some of the incident particle energy is lost into the front detector, before it registers as a valid count in the back detector. The front detector in the HIGH unit is very thin to minimize the energy lost within it, while generating enough signal to operate the coincidence. Thus, while the incident energy of a given particle is not exactly equal to the energy deposited, it is a good approximation.



The histogram count rates in Figures 4b–4d are extracted only for  $B/B_{\text{eq}} < 1.1$  (close to the geomagnetic equator) and centered on  $90^\circ$  local pitch angle ( $\alpha = [80, 100]$  degrees). We note that this local pitch angle and  $B/B_{\text{eq}}$  range maps to roughly  $70^\circ$ – $110^\circ$  equatorial pitch angle and is similar to the selection criteria used in Figure 4a. In a given row, each panel shows the histogram profile accumulated in the given  $L$  range over a 30 day window, the dates of which are indicated above Figure 4b. For example, the first panel in Figure 4b shows the histogram data accumulated in  $L = 2.75$ – $3.05$  in the 30 days centered on 15 April 2013. This time interval is also marked in Figure 4a with a dark blue band near the bottom horizontal axis. Several other 30 day accumulation intervals are considered (columns) and are similarly marked below Figure 4a. We emphasize that the histogram profiles in Figures 4b–4d are not electron flux spectra. They are count rates due to both electron foreground and background counts.

In each panel in Figures 4b–4d, the main channel passband, 0.692–0.793 MeV, is shown with vertical magenta lines and is noted at the right of the figure (as  $\Delta E$ ). The histogram count rates are plotted on different vertical scales in each panel, with the scale range indicated within each panel (" $y = [\dots]$ "). For example, the vertical scale in the first panel in Figure 4b is 0.01–0.04 counts/s. Here the total accumulation window is 30 days, but when restricted to the indicated  $L$ ,  $B/B_{\text{eq}}$ , and pitch-angle range, this amounts to only  $\sim 5000$  s. Thus, the total counts per histogram channel are quite low at this time ( $\sim 100$  counts/channel, i.e.,  $\sim 0.02$  counts/s/channel), which is evidenced by the statistical (Poisson) fluctuations in the histogram profile. Compare this with the histogram profile in Figure 4b after the March 2015 storm (light orange, centered on 5 April 2015), where 0.75 MeV electrons are enhanced in this  $L$  region; the statistical fluctuations are small relative to the large peak in the main channel passband, and the  $y$  axis range is increased by a factor of 20 over the earlier interval. For additional comparison, in the supporting information, we show an analogous plot to Figure 4, but with the same vertical scale on all of the panels in Figures 4b–4d.

Scanning the histogram profiles in Figure 4b reveals several interesting features in this  $L$  range ( $L \approx 2.9$ ). First, we see no evidence of histogram peaks within the main channel passband for the first, third, and fourth time intervals selected (dark blue, cyan, and light green). The second time interval, centered on 13 October 2013 (medium blue), shows a very weak peak in the histogram profile, due to the flux enhancement event observed at this time at the upper edge of this  $L$  range (e.g., Figure 4a). Note that this histogram peak lies at the lower energy edge of the main channel passband ( $\sim 0.7$  MeV), with a steeply falling spectrum within the passband and very little flux evident at 0.8 MeV. Additionally, note that the March 2015 event produced a strong flux enhancement in the outer slot region at this energy (light orange). The fluxes decayed rapidly, however, as there is no histogram peak in the subsequent 30 day interval (dark orange, centered on 5 May 2015). Also, as noted above, following the appearance of ultrarelativistic electrons near  $L = 3$  after the March 2015 event [Baker *et al.*, 2016], Bremsstrahlung contaminates the fluxes, and this contamination is not entirely removed by the standard correction algorithm. The lack of a peak in the dark orange histogram trace, centered on 5 May 2015, confirms that electrons are not detectable here above the background in the main channel energy band, despite Figure 4a suggesting a low, but nonzero, flux.

The histogram profiles in Figure 4c confirm that the March 2015 event produced a strong flux enhancement in the slot region at this energy (light orange). In contrast to the flux decay at higher  $L$ , however, the decay here at lower  $L$  is more gradual, with a histogram peak still evident in the subsequent 30 day time interval (dark orange, centered on 5 May 2015), albeit reduced in intensity by roughly 1 order of magnitude. Additionally, in each of the first four 30 day time intervals selected, the histogram profiles indicate that there are no detectable 0.75 MeV electrons above background levels near the inner edge of the slot ( $L \approx 2.3$ ). Note, however, that Figure 4a suggests that weak flux signatures are observable in this  $L$  region. The lack of a peak in the histogram profiles confirm that these flux signatures are not real and are due to residual contamination that is not entirely removed by the standard correction algorithm. The rapid spacecraft motion and the low foreground levels in this  $L$  range make the standard background corrections challenging in this region, as explained in detail by Claudepierre *et al.* [2015].

The histogram profiles in Figure 4d, extracted near the heart of the inner zone, suggest different electron dynamics from those in the slot region. We see that at the beginning of the interval, in April 2013 (dark blue), the histogram profile is peaked in the main channel passband, with a steeply falling spectrum within the passband. In the subsequent three time intervals (medium blue, cyan, and green), this peak slowly decays, by roughly a factor of 2 over the course of  $\sim 1.5$  years (April 2013 to October 2014). The steeply falling spectrum in the main channel passband in Figure 4d is inferred by comparing with, for example, the light orange

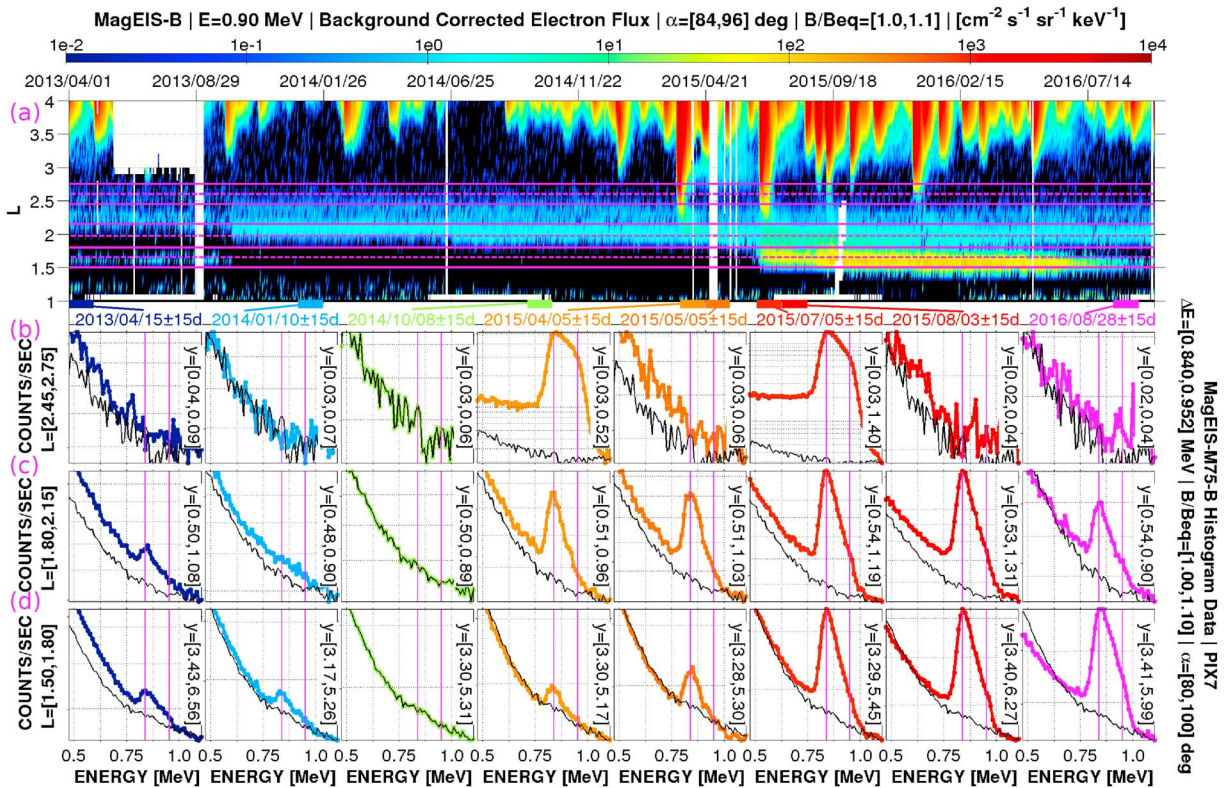


**Figure 5.** Same format as Figure 4, but for 0.90 MeV electrons. (b–d) The histogram profile from 8 October 2014 (light green) is shown as an additional black trace in all of the panels, providing a rough estimate of the background level.

profile in Figure 4b. Also, note that the first four panels in Figure 4c at higher  $L$  show no evidence of flux transport through the slot region and into the inner zone. This evidence may suggest that the 0.75 MeV inner zone population was transported there at an earlier time, prior to April 2013, and slowly and steadily decayed thereafter, as no additional inner zone enhancements are observed until March 2015. However, this transport cannot be confirmed without a detailed examination of the phase-space density at fixed first adiabatic invariant, which is beyond the scope of the present study. Furthermore, note the high background levels in the histogram profiles in the inner zone, likely due to proton contamination. For example, in the first panel of Figure 4d, the low-wing count rate is  $\sim 7$  counts/s and the high-wing count rate is  $\sim 4$  counts/s. Compare this with the corresponding panel in the slot region in Figure 4c, where the wing count rates are an order of magnitude lower ( $\sim 0.1$  counts/s).

Over the entire time interval shown in Figure 4, there are sporadic injections of 0.75 MeV electrons into the slot region, which occasionally penetrate and enhance the inner zone. We emphasize that when considering these data on the whole, we can conclusively say that the March 2015 event transported relativistic electrons through the slot region and into the inner zone (orange profiles), while the early October 2013 event, for example, did not penetrate through the slot region (light blue).

### 3.2. Inner Zone and Slot Region Dynamics: 0.90 MeV

Figure 5 is presented in the same format as Figure 4, but for the 0.90 MeV flux from pixel 7 on MagEIS-B M75, with main channel passband of 0.840–0.952 MeV. The 30 day time windows selected for detailed analysis in Figures 5b–5d are also slightly different from those used in Figure 4. In each of the histogram profiles in Figures 5b–5d, we show an additional black trace, which is the histogram profile from the 8 October 2014 column (light green). This additional black trace in each of the panels serves as a guide to indicate an approximate background level, as there are no discernible peaks in the main channel passband in the 8 October 2014 histogram profiles.

We begin with the histogram profiles in the heart of the slot region ( $L \approx 2.6$ ) in Figure 5b. Here we see flux enhancements following both the March (orange) and June (red) 2015 events. Note that in the subsequent

30 day time intervals following each flux enhancement event, the histogram profiles have decayed to near-background levels, again demonstrating rapid electron losses/decay in the slot region. Both the March and June 2015 flux enhancements are also characterized by an increase in the low-wing count rates, relative to the background profiles (black trace), which is likely due to backscatter. For example, note that in the orange profile in Figure 5b, the count rate in the main channel passband ( $\sim 0.5$  counts/sec) is roughly a factor of 5 larger than the count rate in the low wing ( $\sim 0.1$  counts/sec). This is approximately equal to the  $R$  parameter for this pixel, which is determined as part of the standard background correction algorithm described in Claudepierre *et al.* [2015]. The  $R$  parameter represents the expected ratio of the count rate in the main channel passband to the count rate in the low wing, in the absence of background when foregrounds are high. Thus, this suggests that the enhanced low-wing count rates relative to the background profile (black) are primarily due to backscatter.

The histogram profiles near the outer edge of the inner belt ( $L \approx 2$ , Figure 5c) again indicate that the residual fluxes in Figure 5a are not real. For example, there are no discernible peaks in the 10 January 2014 (cyan) and 8 October 2014 (light green) profiles, while Figure 5a suggests that there is low-intensity flux in this region at these times. We also note that once electrons are enhanced in this  $L$  region following the March and June 2015 events, the decays are observed to be slower than those noted above at higher  $L$ , in the heart of the slot (e.g., compare orange profiles, Figures 5b and 5c). Again, for comparison, we show an analogous plot to Figure 5 in the supporting information, but with the same vertical scale on all of the panels in Figures 5b–5d, so that these dynamics can be compared on the same scale. It is also interesting to note that the first panel in Figure 5c shows a slight peak in the histogram profile, likely the result of an earlier source event into this  $L$  region. This flux is masked in Figure 5a by residual contamination.

In the heart of the inner belt (Figure 5d), we again see evidence of electron transport through the slot to very low  $L$  values following the March and June 2015 events. It is very interesting to note that there is barely a hint of these dynamics in Figure 5a following the March 2015 event. Similarly, the second profile in Figure 5d (cyan) suggests that there is a very low-intensity population of inner-belt electrons at this energy at this time (10 January 2014), a fact that is not at all evident in Figure 5a. We emphasize that a careful examination of the accumulated histogram data reveals inner zone electron signatures that are not captured in the standard background corrected data product. Furthermore, we note that at the end of the interval in Figure 5d (magenta), the histogram data confirm that the electrons transported to this low  $L$  value following the March and June 2015 events are still present. Finally, we note that the abrupt change in character of the inner zone and slot region fluxes in Figure 5a around 2013 October is due to an instrumental reconfiguration and should not be considered physical.

### 3.3. Inner Zone and Slot Region Dynamics: 1.06 MeV

Moving up in energy, Figure 6 shows the 1.06 MeV electron data presented in the same format as Figure 5. These data are from pixel 0 in the MagEIS-B HIGH unit, with the main channel passband of 0.970–1.279 MeV. Figure 6a shows relatively few excursions of 1.06 MeV electrons into the inner slot region, where only the March and June 2015 events result in flux transport into the  $L = 2.15$ – $2.45$  range. It is also clear that 1.06 MeV electrons traverse the slot region and enter the inner zone following the June 2015 event, as noted above. There also appears to be ongoing inward radial transport, where the inner zone flux gradually moves earthward by roughly  $0.2 L$  over the time interval displayed.

The histogram profiles in Figure 6b show features similar to those in the lower-energy channels, namely, a rapid decay of electrons in the slot region and no evidence of inner slot region electrons prior to the March 2015 event. Interestingly, in Figure 6c, we see a very slight bump in the first histogram profile, centered on 15 April 2013 and also in the histogram profiles after the March 2015 event (orange). This suggests that 1.06 MeV electrons were present in the inner belt both at the beginning of the time interval and following the March 2015 event, features that are not at all apparent in Figure 6a. Furthermore, in Figure 6d, we see no evidence of inner zone electrons until the June 2015 event, after which there are very minuscule bumps in the histogram profiles. Nevertheless, this is evidence of low-intensity 1.06 MeV electrons at  $L < 1.5$  at these times. The final, and perhaps most interesting, feature of note is that the histogram data clearly demonstrate that electrons are still present in the inner zone at the end of the time interval (Figures 6c and 6d, magenta), whereas there is no signature of this in Figure 6a. This suggests that the newly formed inner belt persists for at least 1.5 years, from March 2015 up through the end of the time range shown in the plots, September 2016. It is only through



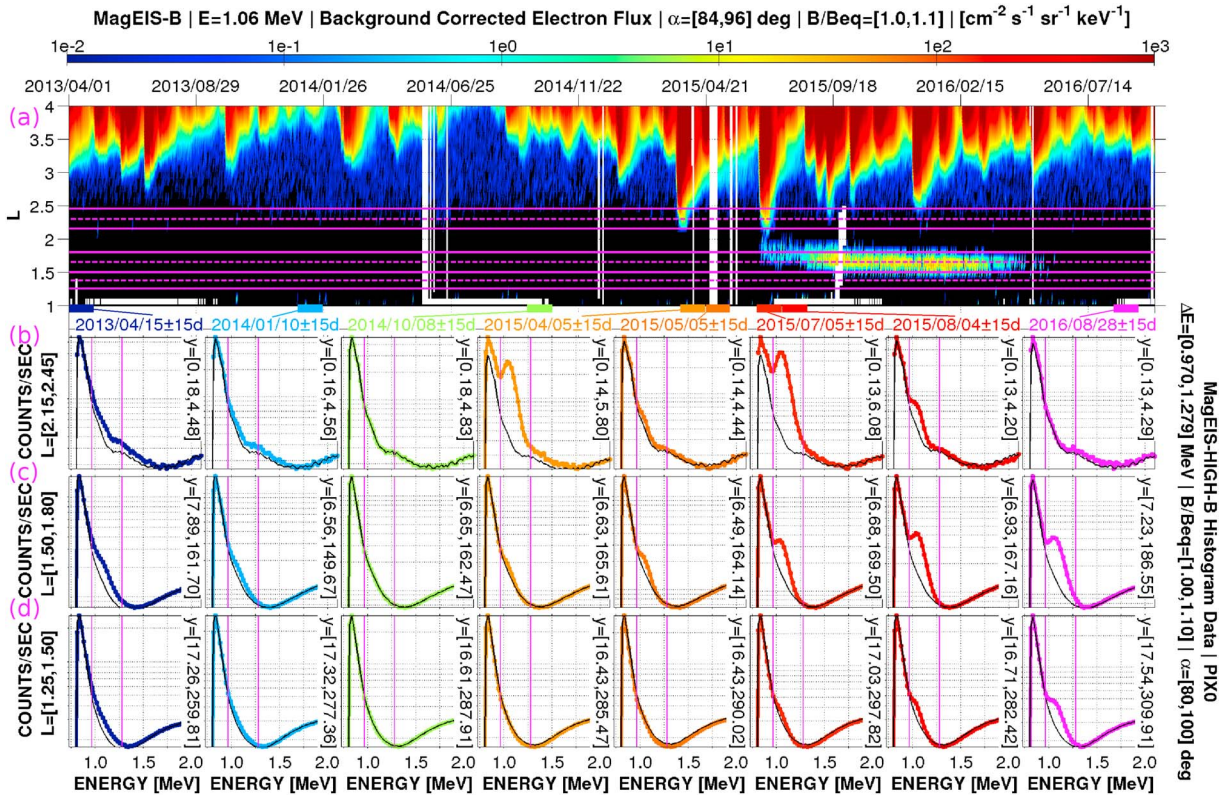


**Figure 6.** Same format as Figure 5, but for 1.06 MeV electrons. Note that many of the features of the newly formed  $\sim 1$  MeV inner belt in Figure 6a are only revealed by examining the histogram data in Figures 6b–6d. For example, we see that low-intensity  $\sim 1$  MeV electrons are present at  $L < 1.8$  in April 2013 (Figure 6c, dark blue); the  $\sim 1$  MeV inner belt formed after the March 2015 event (Figure 6c, orange); the newly formed  $\sim 1$  MeV inner belt is observed up to the end of the time interval displayed (September 2016) and thus persists for at least 1.5 years (Figure 6c, magenta);  $\sim 1$  MeV electrons are present at  $L < 1.5$  in September 2016 (Figure 6d, magenta).

this detailed analysis of the histogram data that we are able to demonstrate that the temporal duration of the newly formed inner belt is much longer than what is suggested in Figure 6a. The reasons for this are not fully understood at this time but will be investigated in follow-on work.

This 1.06 MeV electron channel is the highest energy where we observe electrons in the inner zone over the entire time interval considered, even with the greater sensitivity enabled here by the use of the histogram data (see section 3.4 below). We also emphasize the stability of the proton backgrounds in the inner zone. For example, note that in Figure 6d, prior to March 2015, all of the profiles are nearly identical and dominated by backgrounds. This suggests that the inner-belt protons that produce this contamination are very stable over these timescales.

As noted above, pixel 8 on the M75 unit, with a channel centroid of 1.07 MeV and passband of 1.01–1.17 MeV, provides a complementary measurement to HIGH unit pixel 0. Note that the centroid is nearly identical to that of HIGH pixel 0, but the channel width is much narrower. While background corrections are not possible, at present, on the main channel obtained from M75 pixel 8, we have produced an analogous set of plots to Figures 6b–6d from M75 pixel 8, and these histogram data confirm the conclusions drawn above from the HIGH pixel 0 histogram data in Figures 6b–6d (not shown here).

### 3.4. Inner Zone and Slot Region Dynamics: 1.58 MeV

The final energy we consider is 1.58 MeV, as shown in Figure 7. Figure 7a suggests that 1.58 MeV electrons only penetrate into the outer reaches of the slot region following the March and June 2015 events. The histogram profiles in Figure 7b confirm this and again show a rapid decay of electrons in the slot (see also the analogous figure in the supporting information). Furthermore, Figures 7c and 7d confirm that there are no  $>1.5$  MeV electrons in the inner slot or the inner belt for the entire interval shown. This is the highest energy where we observe any electrons in the slot region, and we find no evidence of electrons at this energy (or higher) in

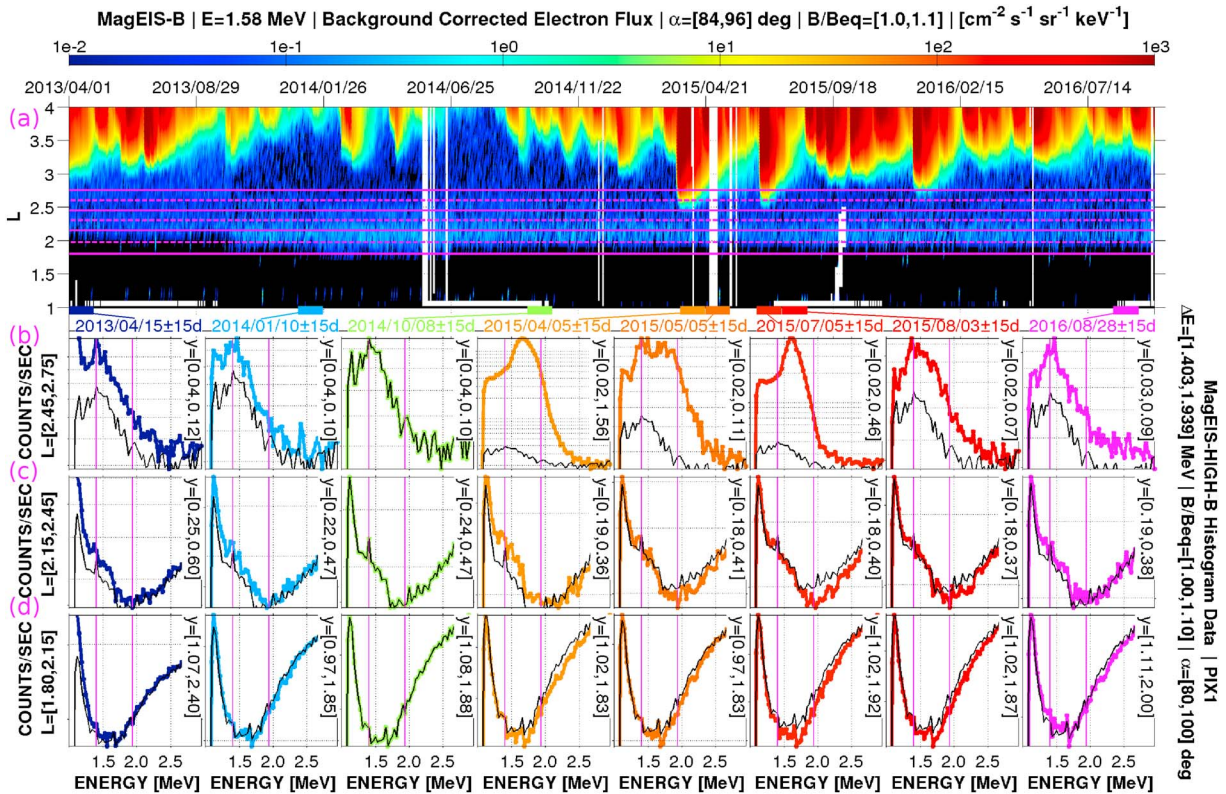


Figure 7. Same format as Figure 5, but for 1.58 MeV electrons.

the inner belt. Also, we again see that the standard correction algorithm leaves a residual band of apparent electrons near the outer edge of the inner belt in Figure 7a. The histogram profiles in Figure 7d confirm that these are not real electrons.

Finally, we note that the HIGH unit histogram profile shapes (Figures 6b–6d and 7b–7d) are considerably different from those of M75 (Figures 4b–4d and 5b–5d), particularly in the low-wing range. For example, when the histogram profiles are entirely due to background and do not show peaks in the main channel passbands, the M75 profiles are monotonically decreasing with energy (e.g., Figure 5d, light green), while the HIGH unit profiles are concave up (first decreasing with energy and then increasing; e.g., Figure 7d, light green). A number of factors likely contribute to these differences, such as the use of detector coincidence in the HIGH unit, the stronger magnetic field within the HIGH unit, and the larger amount of shielding surrounding the HIGH unit [Blake *et al.*, 2013]. Understanding these differences will be the subject of future work.

#### 4. Attempts to Estimate an Upper Limit for Inner Zone ~MeV Electron Flux

Fennell *et al.* [2015] placed an upper limit on ~1 MeV electron flux at  $L = 1.5$  of ~0.1 electrons/( $\text{cm}^2 \text{ s sr keV}$ ). Here “upper limit” refers to an upper limit on the electron flux intensity that could potentially be present during a given observation interval (i.e., not a physical limit on what flux levels are possible). Fennell *et al.* [2015] calculated their upper limit estimate by accumulating data in the inner zone over a roughly 1 week quiet interval, and then analyzing it with an alternative background correction technique. This technique, which we refer to as the “fully Bayesian-Poisson” or “fullBP” method, is described briefly below and in greater detail in an Aerospace Corp. technical report [O’Brien and Claudepierre, 2015]. One of the original goals of the present study was to quantify more precisely the upper limit of inner zone MeV electron flux obtained by Fennell *et al.* [2015], by accumulating over a longer time interval (e.g., 1000 days) and applying the same fullBP method. We now report on those efforts, which produced ambiguous results and, thus, were largely unsuccessful.

#### 4.1. The Fully Bayesian-Poisson Background Correction Method

Whereas the standard background correction method described in *Claudepierre et al.* [2015] simply subtracts an estimated background from the observed counts, the fullBP method accounts for the possibility that, due to Poisson counting statistics, the subtraction sometimes gives invalid, negative answers. The goal of the fullBP method is to obtain the posterior distribution of the true main channel foreground count rate and, therefore, the foreground flux.

The fullBP method uses the same model of the background as the standard method, which begins with the observed low-wing ( $c_a$ ), high-wing ( $c_b$ ), and main channel counts (e.g., Figure 1), where we use the same notation as *Claudepierre et al.* [2015]. The main channel counts, denoted as  $Q'$ , can be taken from the main rate data or derived from the downsampled histogram data ( $C'$ ), as described above in section 1. For this study, the main channel counts are obtained by summing the histogram counts in the channel passband, and thus, we assume  $Q' = C'$ . We denote the foreground count rate per pulse-height channel in the passband as  $C_0$ . The background count rate,  $I_p$ , in pulse-height channel  $p$  is assumed to vary as an exponential with respect to pulse-height channel, from the low wing to the high wing. Explicitly,  $I_p = I_0 m^p$ , where  $m$  is the slope of the background in the channel passband and  $p \in [a, b]$  (e.g., Figure 1).

The low wing is assumed to include background and a fraction,  $1/R$ , of the foreground due to backscatter. The  $R$  factor was introduced earlier and is estimated from times and locations when the background is thought to be negligible [e.g., near apogee; *Claudepierre et al.*, 2015]. The high wing is assumed to be pure background. In this formulation, then, the expected number of counts in the low wing is  $\langle c_a \rangle = [I_a + C_0/R]n_a T$ ; the high wing is  $\langle c_b \rangle = I_b n_b T$ , and the main channel is  $\langle Q' \rangle = \langle C' \rangle = [N' C_0 + \sum I_p]T$ , where  $I_a$  is the count rate in pulse-height channel  $a$  and  $I_b$  is the count rate in pulse-height channel  $b$ . The constants  $n_a$ ,  $n_b$ , and  $N'$  count the number of pulse-height channels in the low wing, high wing, and main channel, respectively;  $T$  is the histogram integration time; and the sum,  $\sum I_p$ , is taken over the pulse-height channels that contribute to the main channel ( $[j, k]$ ). We thus have three related Poisson processes:  $c_a$ ,  $c_b$ , and  $Q'$ . To compute the posterior estimate of  $C_0$ , we must establish priors for all of the unknown parameters:  $C_0$ ,  $I_0$ , and  $m$ . For  $C_0$  and  $I_0$ , we assume that all positive values are equally likely and negative values are not allowed. For  $m$ , we assume that the prior distribution is proportional to  $m$  and in the domain  $[0, 1]$ . That is, we assume that a flat background ( $m \sim 1$ ) is somewhat more likely than a very steep background ( $m \sim 0$ ). (We note that under some circumstances, we have to assume a linear, rather than exponential background across the passband, but the rest of the calculation is the same as for the exponential,  $I_0 m^p$ ).

The goal now is to compute the distribution of the true main channel counts,  $p(C_0 | c_a, c_b, Q')$ , given the observed parts of the histogram,  $c_a$ ,  $c_b$ , and  $Q'$ . In order to do this, we use the prior distribution  $p(C_0, I_0, m) \propto m/2$ , as outlined above, along with independent Poisson probabilities of the form  $p(y | \langle y \rangle) = \langle y \rangle^y \exp[-\langle y \rangle]/y!$  for each of the observed counts  $c_a, c_b, Q'$ . The joint probability distribution of all the variables is then

$$p(C_0, I_0, m, c_a, c_b, Q') = p(C_0, I_0, m) p(c_a | \langle c_a \rangle) p(c_b | \langle c_b \rangle) p(Q' | \langle Q' \rangle) \quad (1)$$

Finally, we have

$$p(C_0 | c_a, c_b, Q') = \frac{p(C_0, c_a, c_b, Q')}{p(c_a, c_b, Q')} = \frac{\int \int p(C_0, I_0, m, c_a, c_b, Q') dm dI_0}{\int \int \int p(C_0, I_0, m, c_a, c_b, Q') dm dI_0 dC_0} \quad (2)$$

These integrals are carried out numerically to obtain the posterior distribution,  $p(C_0 | c_a, c_b, Q')$ . From that distribution we can compute the median, 95th, and 99th percentiles. We can then scale these counts-percentiles to flux using the flux conversion factor and time duration of the samples. We interpret the 95th and 99th percentiles as two estimates of the upper limit foreground flux, and the median approximates the nominal value of the flux. When these three percentiles collapse to a similar value, this indicates that we have a well-constrained value of the flux. When they do not, we are unable to resolve any finite foreground. A complete derivation, as well as discussion of the numerical integration methods, can be found in *O'Brien and Claudepierre* [2015].

Unfortunately, the numerical integrals above are computationally very intensive. Therefore, we cannot perform the fullBP analysis routinely. Also, as will be discussed below, the entire method breaks down when the energy channel width is large, as in the HIGH unit, as the assumption of an exponential interpolation ( $I_0 m^p$ ) of the background through the passband breaks down (see, e.g., Figure 7d). This breakdown also affects our standard background correction algorithm, which also assumes an exponential background.



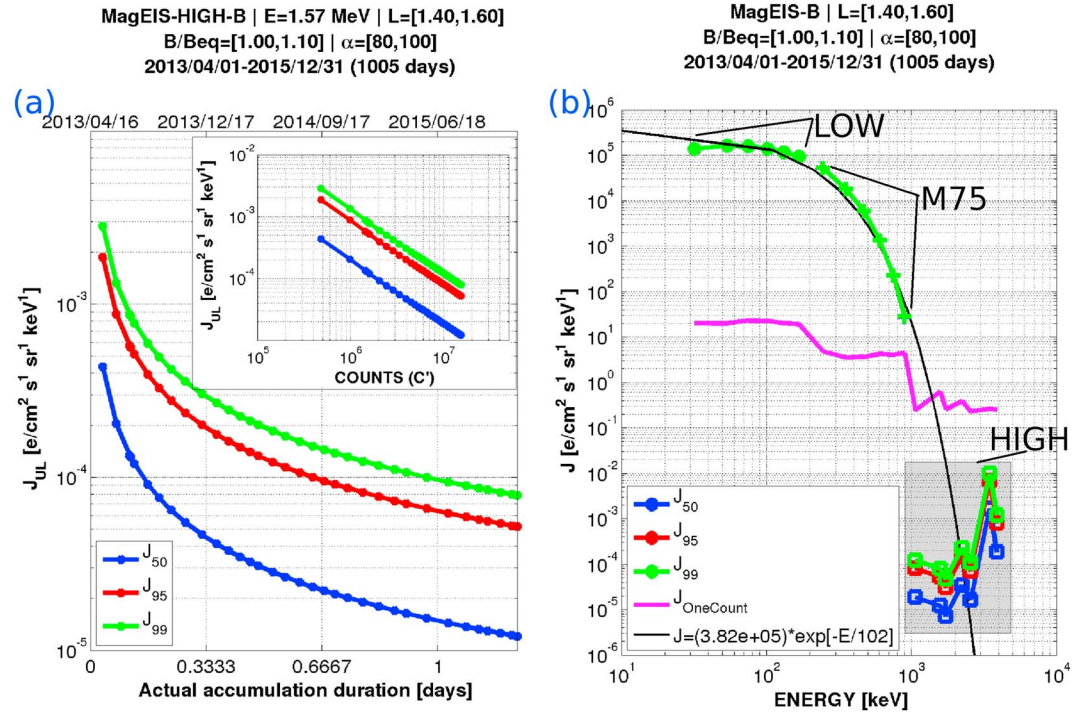


**Figure 8.** (a) The result of the fully Bayesian-Poisson (fullBP) algorithm applied to the 1.58 MeV channel from MagEIS-B HIGH. These data were continuously accumulated over 1005 days (1 April 2013 through 31 December 2015) in the near-equatorial inner zone ( $L = 1.4$ – $1.6$ ,  $B/B_{eq} < 1.1$ ) near  $90^\circ$  local pitch angle. The 50th-, 95th-, and 99th-percentile upper limit flux estimates ( $J_{UL}$ ) are plotted versus the accumulation time, which ranges from 0 to 1.2 days, subject to the  $L$ ,  $B/B_{eq}$ , and pitch-angle constraints. The corresponding UTC times are shown along the top horizontal axis for the entire 1005 day interval. The inset panel shows the same data plotted versus main channel counts,  $C'$ . (b) The flux spectrum obtained from the fullBP procedure on all available MagEIS energy channels (LOW, M75, and HIGH) subject to the same  $L$ ,  $B/B_{eq}$ , and pitch-angle constraints. The one-count flux level for the entire 1005 day accumulation interval is shown in magenta, and an exponential fit to the LOW and M75 data is shown in black. On the whole, the figure shows that the fullBP procedure fails to produce valid upper estimates on the inner zone MeV electron flux, as the estimates obtained from the HIGH unit decrease with increasing accumulation time.

#### 4.2. Results From the Fully Bayesian-Poisson Method

Figure 8 shows results from the fullBP calculation using electron data from the 1.58 MeV channel from the MagEIS-B HIGH unit. The primary panel in Figure 8a shows the upper limit flux estimates ( $J_{UL}$ ) plotted versus the accumulation time, which ranges from 0 to 1.2 days, subject to the  $L$ ,  $B/B_{eq}$  and pitch-angle constraints. The corresponding UTC times are shown along the top horizontal axis for the entire 1005 day interval. These data were accumulated every time MagEIS-B HIGH was in the  $L = 1.4$ – $1.6$  range, near the magnetic equator ( $B/B_{eq} < 1.1$ ) and near  $90^\circ$  local pitch angle ( $\alpha = 80$ – $100^\circ$ ). The three traces shown in the main panel are the 50th-, 95th-, and 99th-percentile upper limit flux estimates,  $J_{UL}$ , obtained as described above. We see that as we continuously accumulate more and more counts, the upper limit estimates steadily decrease and do not asymptote toward any particular value. This suggests that the upper limit flux estimates will continue to decrease as we accumulate over even longer time intervals. More importantly, the three percentiles do not collapse to a single value, which indicates that the fullBP technique is unable to detect a valid upper limit, in this case. The inset panel in Figure 8a shows the same data, but plotted against main channel counts,  $C'$ . Again, as we accumulate more counts, we do not see any evidence of the upper limit estimates asymptoting to a common value. Thus, the upper limit estimates from this energy channel and in this  $L$  region produce ambiguous results, as the upper limit estimate obtained depends solely on the accumulation time/counts accumulated, because there is apparently no foreground signal.

Figure 8b presents a flux spectrum obtained from the upper limit calculations described in Figure 8a. To obtain the spectrum in Figure 8b, we repeat the fullBP procedure (accumulating over 1005 days) for each MagEIS energy channel, using data from all three MagEIS units, LOW, M75, and HIGH. For example, the three flux values shown in Figure 8b at 1.58 MeV are the three values in Figure 8a at the end of the time interval:  $J_{99} \approx 8 \times 10^{-5}$ ,

$J_{95} \approx 5 \times 10^{-5}$ , and  $J_{50} \approx 1 \times 10^{-5}$  electrons/(cm<sup>2</sup> s sr keV). In Figure 8b, the six LOW unit channels are shown as solid dots, the six M75 channels are shown as plus symbols (+), and the seven HIGH unit channels are shown as open squares. We also show the flux value that corresponds to one count accumulated in each energy channel over the 1005 days (magenta trace). The black trace in Figure 8b shows an exponential fit to the LOW and M75 data only, with the fit parameters indicated in the panel legend.

There are several features of note in Figure 8b. First, we see that for the LOW and M75 energy channels, the 50th-, 95th-, and 99th-percentile upper limit flux estimates from the fullBP calculation all lie on top of one another. As noted above, this indicates that the distribution has collapsed and that the  $J_{UL}$  values obtained represent well-constrained flux estimates. This lends confidence that the fullBP procedure performs as expected when there are significant foreground fluxes in the main channel passband, relative to the background. Second, we note that this is not the case for the seven HIGH unit channels, which are highlighted by the shaded box. The upper limit flux estimates do not collapse to a single value, as we demonstrated in detail for the 1.58 MeV channel in Figure 8a. It is clear, based on the discussion above, that the flux levels here will simply continue to decrease as we accumulate over longer and longer time intervals. Thus, these flux levels have ambiguous meaning and cannot be considered to be valid upper limits on the inner zone electron flux, as the intensity depends on the accumulation time. The best we can do, at present, is say that the  $>1$  MeV inner zone electron flux must be less than the one count estimate, providing an upper limit of  $\sim 0.1$  electrons/(cm<sup>2</sup> s sr keV), which is the same value obtained by Fennell *et al.* [2015].

We emphasize that the histogram profiles in Figures 6c and 6d suggest a low level of 1.06 MeV flux in the  $L = 1.4 - 1.6$  range considered in Figure 8. This low-intensity population is not captured by the fullBP procedure, as Figure 8b indicates. If this low-intensity population were captured, the three percentiles would collapse to a single value at 1.06 MeV. This failure of the fullBP procedure on the HIGH unit data is likely due to both the shape of the histogram profiles and the wide energy channel passbands. Specifically, in Figures 6c and 6d, we see that the background is not a straight line across the channel passband as noted above. The profiles are concave up, so that a linear interpolation between the low and high wings will mask and zero out any low-intensity signal peak in the channel passband. Here our assumption of a straight line background in log-linear space is inadequate, as it takes a significant flux level to overcome this concavity deficit in the HIGH unit. The fullBP algorithm (and the standard algorithm) sees a deficiency in counts from what it expects, due to the straight-line background assumption. Thus, it calculates a much lower upper limit estimate than what is to be expected. Compare this with the inner zone histogram profiles from the M75 unit (e.g., Figure 5d), where the background profiles are more linear across the narrower channel passbands. The fullBP procedure is thus better able to capture the low-intensity flux levels at 0.90 MeV in the inner zone (e.g., Figure 8b).

While it is undesirable that the concavity in the HIGH unit histogram data leads to a rejection of valid foreground fluxes when there is a very small peak in the passband, it is nevertheless a feature of the fullBP algorithm (and the standard correction algorithm), as designed. Thus, when the foreground signals are low, the true flux is slightly underestimated. The low-intensity population of 1.06 MeV electrons in the inner zone is only revealed by carefully examining the HIGH unit histogram data. While we can convert these histogram counts to flux, we cannot estimate and correct for the background contamination, with either the standard or the fullBP method. Thus, we can only confirm the presence of these electrons in the inner zone and cannot, at this time, quantify their true intensity level. To do that, we would need an independent estimate of the expected background shape in the HIGH unit histograms. We have begun to experiment with empirically determined background profiles, but have yet to employ them, as we have not yet validated them against instrument simulations and onboard penetrating proton measurements. These efforts will be the focus of follow-on work.

## 5. Conclusions and Summary

We have presented a detailed analysis of relativistic electron observations in the inner zone and slot region from the MagEIS instrument on Van Allen Probes. We have demonstrated that  $\sim 1$  MeV electrons were transported into the inner zone following the March and June 2015 events, creating a new inner belt that persisted for at least 1.5 years. At the time of writing, this is the only injection of  $>1$  MeV electrons into the inner zone observed during the Van Allen Probes era. This long-lasting inner belt is contrasted with slot region injections, which occur more frequently but decay rapidly, on the order of tens of days. Additionally, we find no evidence of  $>1.5$  MeV electrons in the inner zone during the entire time interval considered (April 2013 through

September 2016). We note that  $>1.5$  MeV electrons have been reported in the inner zone and slot region in previous studies [Blake *et al.*, 1992; Baker *et al.*, 2004; Looper *et al.*, 2005]. However, the electron measurements described in Baker *et al.* [2004] and Looper *et al.* [2005] have recently been called into question by Selesnick [2015b]. He argues that these inner zone measurements are not the signature of multi-MeV electrons, but rather chance coincidences between inner-belt protons and lower-energy electrons, again highlighting the challenging nature of interpreting inner zone observations.

We have made use of the background corrected MagEIS main channel data, along with detailed pulse-height spectra from the histogram data, to validate and confirm our findings. We emphasize that the electron dynamics in the inner zone and slot region can be obscured, or “hidden,” by background contamination. We have shown that the true dynamics of inner zone/slot region electrons are revealed only after the background corrections have been applied (e.g., compare Figure 2 with Figure 3). For example, the injection of 1.06 MeV electrons into the inner zone following the June 2015 storm is clearly observed in Figure 3, while in Figure 2, it is obscured by high levels of inner zone proton contamination. Additionally, Figure 3 shows that the 0.75 MeV electrons decay very slowly in the inner zone (before the March and June 2015 events), whereas this fact is hardly evident in Figure 2. Also, while it is well known that the inner zone is subject to high levels of penetrating backgrounds that can overwhelm particle measurements, the slot region, too, can experience background contamination [e.g., Kronberg *et al.*, 2016]. Bremsstrahlung background from ultrarelativistic electrons can obscure the low foreground signals in this region of the space environment. This subtle effect was noted above and can manifest itself, for example, as differences in slot region decay rates that are obtained when using uncorrected versus corrected data [e.g., Drozdov *et al.*, 2015].

In addition, it was shown that some inner zone and slot region features are not revealed even in the standard background corrected data. The background correction algorithm itself can obscure and remove subtle signals that are only revealed when carefully examining the histogram data. A detailed analysis of the histogram data both confirmed our results and also revealed low-intensity inner zone and slot region electrons that are not captured in the standard background corrected data product. In this regard, we note that the standard correction algorithm was designed to be conservative. Thus, we expect, for example, that the flux intensity, radial extent, and temporal duration of the new  $\sim 1$  MeV inner belt (e.g., Figure 6a) are all underestimated. This will be explored in follow-on work using an alternative method to estimate and remove background contamination that is currently under development, but the results of which are too preliminary to describe here. Finally, we briefly discussed efforts to refine the upper limit of inner zone MeV electron flux levels obtained in earlier work. These efforts were largely unsuccessful, as they were unable to detect any foreground at all in the HIGH unit.

In this paper we have avoided any discussion on the mechanisms that result in relativistic electron enhancements in the inner zone and slot region. Similarly, while noted, we did not investigate the physical processes that lead to the observed differences in the rapid slot region decays, when compared with the slower, more gradual decays observed in the inner zone. Such analyses are reserved for future work. Instead, our goal is to provide a clear presentation of the MagEIS electron data in these low  $L$  regions of geospace and offer multiple lines of supporting evidence to validate the background corrected observations. Finally, we have demonstrated that care must be exercised even when using background corrected MagEIS data to study relativistic electron dynamics in the inner zone and slot region, due to contamination that masks the true dynamics of these particles. Now that we have established how to work with these data, we can use them in more specialized products, such as pitch-angle distributions and phase-space density profiles, as we investigate the physical mechanisms that drive relativistic electron dynamics in the inner belt and slot region.

#### Acknowledgments

This work was supported by RBSP-ECT funding provided by JHU/APL contract 967399 under NASA's Prime contract NAS5-01072. Work at JHU/APL was supported by NASA grant NNX10AK93G. All of the “release 3 (rel03)” level 2+ MagEIS data used in this manuscript are in the public domain and accessible from the Van Allen Probes Science Gateway. Level 1 MagEIS histogram data can be made available by contacting the lead author (SGC). We acknowledge use of NASA/GSFC's Space Physics Data Facility's CDAWeb service and OMNI data. One author (SGC) would like to thank Jeremy Faden and all of the developers of Autoplot.

#### References

- Albert, J. M., M. J. Starks, R. B. Horne, N. P. Meredith, and S. A. Glauert (2016), Quasi-linear simulations of inner radiation belt electron pitch angle and energy distributions, *Geophys. Res. Lett.*, **43**, 2381–2388, doi:10.1002/2016GL067938.
- Baker, D. N., S. G. Kanekal, X. Li, S. P. Monk, J. Goldstein, and J. L. Burch (2004), An extreme distortion of the Van Allen belt arising from the ‘Halloween’ solar storm in 2003, *Nature*, **432**, 878–881, doi:10.1038/nature03116.
- Baker, D. N., et al. (2016), Highly relativistic radiation belt electron acceleration, transport, and loss: Large solar storm events of March and June 2015, *J. Geophys. Res. Space Physics*, **121**, 6647–6660, doi:10.1002/2016JA022502.
- Blake, J. B., W. A. Kolasinski, R. W. Fillius, and E. G. Mullen (1992), Injection of electrons and protons with energies of tens of MeV into  $L < 3$  on 24 March 1991, *Geophys. Res. Lett.*, **19**, 821–824, doi:10.1029/92GL00624.
- Blake, J. B., et al. (2013), The magnetic electron ion spectrometer (MagEIS) instruments aboard the radiation belt storm probes (RBSP) spacecraft, *Space Sci. Rev.*, **179**, 383–421, doi:10.1007/s11214-013-9991-8.



- Bostrom, C. O., D. S. Beall, and J. C. Armstrong (1970), Time history of the inner radiation zone, October 1963 to December 1968, *J. Geophys. Res.*, **75**, 1246–1256, doi:10.1029/JA075i007p01246.
- Cladis, J. B., G. T. Davidson, and L. L. Newkirk (1973), The trapped radiation handbook, Tech. Rep. AD-738841, Lockheed Palo Alto Research Laboratory, Palo Alto, Calif.
- Claudepierre, S. G., et al. (2015), A background correction algorithm for Van Allen Probes MagEIS electron flux measurements, *J. Geophys. Res. Space Physics*, **120**, 5703–5727, doi:10.1002/2015JA021171.
- Drozdzov, A. Y., Y. Y. Shprits, K. G. Orlova, A. C. Kellerman, D. A. Subbotin, D. N. Baker, H. E. Spence, and G. D. Reeves (2015), Energetic, relativistic, and ultrarelativistic electrons: Comparison of long-term VERB code simulations with Van Allen Probes measurements, *J. Geophys. Res. Space Physics*, **120**, 3574–3587, doi:10.1002/2014JA020637.
- Farley, T. A. (1969), Radial diffusion of electrons at low L values, *J. Geophys. Res.*, **74**, 377–380, doi:10.1029/JA074i001p00377.
- Fennell, J. F., S. G. Kanekal, and J. L. Roeder (2012), Storm responses of radiation belts during solar cycle 23: HEO satellite observations, in *Dynamics of the Earth's Radiation Belts and Inner Magnetosphere*, *Geophys. Monogr. Ser.*, vol. 199, edited by D. Summers et al., pp. 371–384, AGU, Washington, D. C., doi:10.1029/2012GM001356.
- Fennell, J. F., J. L. Roeder, W. S. Kurth, M. G. Henderson, B. A. Larsen, G. Hospodarsky, J. R. Wygant, J. S. G. Claudepierre, J. B. Blake, H. E. Spence, J. H. Clemmons, H. O. Funsten, C. A. Kletzing, and G. D. Reeves (2014), Van Allen Probes observations of direct wave-particle interactions, *Geophys. Res. Lett.*, **41**, 1869–1875, doi:10.1002/2013GL059165.
- Fennell, J. F., S. G. Claudepierre, T. P. O'Brien, J. B. Blake, J. H. Clemmons, H. E. Spence, and G. D. Reeves (2015), Van Allen Probes show the inner radiation zone contains no MeV electrons: ECT/MagEIS data, *Geophys. Res. Lett.*, doi:10.1002/2014GL062874.
- Kronberg, E. A., et al. (2016), Contamination in electron observations of the silicon detector on board Cluster/RAPID/IES instrument in Earth's radiation belts and ring current, *Space Weather*, **14**, 449–462, doi:10.1002/2016SW001369.
- Li, X., R. S. Selesnick, D. N. Baker, A. N. Jaynes, S. G. Kanekal, Q. Schiller, L. Blum, J. Fennell, and J. B. Blake (2015), Upper limit on the inner radiation belt MeV electron intensity, *J. Geophys. Res. Space Physics*, **120**, 1215–1228, doi:10.1002/2014JA020777.
- Looper, M. D., J. B. Blake, and R. A. Mewaldt (2005), Response of the inner radiation belt to the violent Sun-Earth connection events of October-November 2003, *Geophys. Res. Lett.*, **32**, L03506, doi:10.1029/2004GL021502.
- Lyons, L. R., and R. M. Thorne (1973), Equilibrium structure of radiation belt electrons, *J. Geophys. Res.*, **78**, 2142–2149, doi:10.1029/JA078i013p02142.
- Mauk, B. H., N. J. Fox, S. G. Kanekal, R. L. Kessel, D. G. Sibeck, and A. Ukhorskiy (2013), Science objectives and rationale for the radiation belt storm probes mission, *Space Sci. Rev.*, **179**, 3–27, doi:10.1007/s11214-012-9908-y.
- Newkirk, L. L., and M. Walt (1968a), Radial diffusion coefficient for electrons at  $1.76 < L < 5$ , *J. Geophys. Res.*, **73**, 7231–7236, doi:10.1029/JA073i023p07231.
- Newkirk, L. L., and M. Walt (1968b), Radial diffusion coefficient for electrons at low L values, *J. Geophys. Res.*, **73**, 1013–1017, doi:10.1029/JA073i003p01013.
- O'Brien, T. P., and S. G. Claudepierre (2015), Fully Bayesian-Poisson calculation of electron foreground count rate for the MagEIS instrument, Tech. Rep. ATR-2015-00906, Aerospace Corp., Los Angeles, Calif.
- O'Brien, T. P., S. G. Claudepierre, T. B. Guild, J. F. Fennell, D. L. Turner, J. B. Blake, J. H. Clemmons, and J. L. Roeder (2016), Inner zone and slot electron radial diffusion revisited, *Geophys. Res. Lett.*, **43**, 7301–7310, doi:10.1002/2016GL069749.
- Olson, W. P., and K. A. Pfizter (1977), Magnetospheric magnetic field modeling, Tech. Rep. Annu. Report, McDonnell-Douglas Astronautics Co., Huntington Beach, Calif.
- Reeves, G. D., et al. (2016), Energy-dependent dynamics of keV to MeV electrons in the inner zone, outer zone, and slot regions, *J. Geophys. Res. Space Physics*, **121**, 397–412, doi:10.1002/2015JA021569.
- Rosen, A., and N. L. Sanders (1971), Loss and replenishment of electrons in the inner radiation zone during 1965-1967, *J. Geophys. Res.*, **76**, 110–121, doi:10.1029/JA076i001p00110.
- Schulz, M., and L. J. Lanzerotti (1974), *Particle Diffusion in the Radiation Belts, Physics and Chemistry in Space*, vol. 7, 215 pp., Springer, New York.
- Selesnick, R. S. (2012), Atmospheric scattering and decay of inner radiation belt electrons, *J. Geophys. Res.*, **117**, A08218, doi:10.1029/2012JA017793.
- Selesnick, R. S. (2015a), High-energy radiation belt electrons from CRAND, *J. Geophys. Res. Space Physics*, **120**, 2912–2917, doi:10.1002/2014JA020963.
- Selesnick, R. S. (2015b), Measurement of inner radiation belt electrons with kinetic energy above 1 MeV, *J. Geophys. Res. Space Physics*, **120**, 8339–8349, doi:10.1002/2015JA021387.
- Selesnick, R. S. (2016), Stochastic simulation of inner radiation belt electron decay by atmospheric scattering, *J. Geophys. Res. Space Physics*, **121**, 1249–1262, doi:10.1002/2015JA022180.
- Selesnick, R. S., Y.-J. Su, and J. B. Blake (2016), Control of the innermost electron radiation belt by large-scale electric fields, *J. Geophys. Res. Space Physics*, **121**, 8417–8427, doi:10.1002/2016JA022973.
- Su, Y.-J., R. S. Selesnick, and J. B. Blake (2016), Formation of the inner electron radiation belt by enhanced large-scale electric fields, *J. Geophys. Res. Space Physics*, **121**, 8508–8522, doi:10.1002/2016JA022881.
- Tomassian, A. D., T. A. Farley, and A. L. Vampola (1972), Inner-zone energetic-electron repopulation by radial diffusion, *J. Geophys. Res.*, **77**, 3441–3454, doi:10.1029/JA077i019p03441.
- Turner, D. L., et al. (2015), Energetic electron injections deep into the inner magnetosphere associated with substorm activity, *Geophys. Res. Lett.*, **42**, 2079–2087, doi:10.1002/2015GL063225.
- West, H. I., Jr., and R. M. Buck (1976), A study of electron spectra in the inner belt, *J. Geophys. Res.*, **81**, 4696–4700, doi:10.1029/JA081i025p04696.
- Zhao, H., and X. Li (2013), Modeling energetic electron penetration into the slot region and inner radiation belt, *J. Geophys. Res. Space Physics*, **118**, 6936–6945, doi:10.1002/2013JA019240.
- Zhao, H., X. Li, J. B. Blake, J. F. Fennell, S. G. Claudepierre, D. N. Baker, A. N. Jaynes, D. M. Malaspina, and S. G. Kanekal (2014a), Peculiar pitch angle distribution of relativistic electrons in the inner radiation belt and slot region, *Geophys. Res. Lett.*, **41**, 2250–2257, doi:10.1002/2014GL059725.
- Zhao, H., X. Li, J. B. Blake, J. F. Fennell, S. G. Claudepierre, D. N. Baker, A. N. Jaynes, and D. M. Malaspina (2014b), Characteristics of pitch angle distributions of hundreds of keV electrons in the slot region and inner radiation belt, *J. Geophys. Res. Space Physics*, **119**, 9543–9557, doi:10.1002/2014JA020386.